

# Transient characteristics of a solid oxide electrolysis cell under different voltage ramps: Transport phenomena behind overshoots

Zhaojian Liang<sup>a</sup>, Jingyi Wang<sup>b,1</sup>, Yang Wang<sup>c,d</sup>, Meng Ni<sup>d</sup>, Mengying Li<sup>a,\*</sup>

<sup>a</sup> Department of Mechanical Engineering & Research Institute for Smart Energy, The Hong Kong Polytechnic University, Hong Kong Special Administrative Region

<sup>b</sup> School of Science, Harbin Institute of Technology, Shenzhen, 518055, China

<sup>c</sup> State Key Laboratory of Engines, Tianjin University, 135 Yaguan Road, Tianjin 300350, China

<sup>d</sup> Department of Building and Real Estate, Hong Kong Polytechnic University, Hung Hom, Kowloon, Hong Kong, China

## ARTICLE INFO

### Keywords:

Hydrogen production  
Water splitting  
Solid oxide cell  
Transient simulation  
Dynamic response  
Transport phenomena

## ABSTRACT

A promising solution to the storage of intermittent renewable energy is to integrate solid oxide electrolysis cells (SOEC) with solar/wind power. This trend necessitates comprehensive, quantitative investigations on the transient characteristics of SOEC, especially under varying power-supply conditions. For this purpose, a high-resolution, 3-dimensional, transient numerical model, as well as an adaptive time-stepping strategy, is proposed in this study. This study analyzes the electrical, gaseous, and thermal responses of SOEC to voltage ramps with different ramp rates and ramp magnitudes. The results show that electrical undershoots or overshoots occur after fast voltage changes. This phenomenon reflects the discrepancies between the steady and transient current–voltage characteristics and may lead to unsteady hydrogen production rates in practice. The electrical undershoots or overshoots are caused by the different transfer rates in SOEC – electronic/ionic transfer rate is faster than mass transfer rate, and mass transfer rate is faster than heat transfer rate. Furthermore, the electrical undershoots or overshoots can be divided into two parts. One part is related to mass-transfer lag, and the other part is related to heat-transfer lag. The former can be alleviated or eliminated by simply slowing down the voltage ramp, while the latter needs a more effective control strategy other than merely adjusting the voltage ramps. Apart from the electrical conditions, cell structure also has significant impacts on the electrical responses, e.g., the rib and the length of channel are related to the non-uniform electrical responses in the functional layer. Finally, via a quantitative technique developed from linear time-invariant systems, it is shown that the electrical responses of SOEC are governed by two time constants in the functional layer, namely the mass-transfer time constant (estimated as  $\tau_{m,H_2O,FL} = 0.00723$  s) and the heat-transfer time constant (estimated as  $\tau_{t,FL} = 180$  s).

## 1. Introduction

It is expected that renewable energy (e.g., solar and wind energy) will play an important role in the future power grid to cope with the increasingly serious climate problems and energy crisis. In 2021, solar and wind power exceeded 10% share of the global power generation with a rapid annual growth of 226 GW in capacity [1]. Despite of the fast development in installed capacity, solar and wind power, due to their time-varying nature, are still facing a practical issue of uncertain power output, which is a burden to the stability of the power grid. An efficient solution to cope with the intermittence of renewable energy is energy storage — storing excess electric power in the forms of other energies, such as mechanical, thermal and chemical. As such, the long-term energy storage in the form of hydrogen [2] gains growing interests

since the utilization of hydrogen is convenient, clean, and efficient via fuel cells or traditional combustion [3].

Hydrogen can be produced by integrating water electrolysis with solar or wind power [4,5]. In this way, the whole process from power generation to energy storage and utilization is carbon-free. When compared to mature electrolysis technologies, such as alkaline and Polymer electrolyte membrane (PEM) electrolysis with power consumption of around 56 kWh/kg H<sub>2</sub>, solid oxide electrolysis cells (SOEC) shows a superior efficiency with 42 kWh/kg H<sub>2</sub> [6] power consumption owing to its high operating temperature (500 °C to 1000 °C) [7]. Although a number of studies hold optimistic views on the integrated solar–SOEC system in terms of the economical viability [8] and the high solar-to-hydrogen (STH) efficiency [3], there are some concerns on the technical

\* Corresponding author.

E-mail addresses: [wangjingyi@hit.edu.cn](mailto:wangjingyi@hit.edu.cn) (J. Wang), [mengying.li@polyu.edu.hk](mailto:mengying.li@polyu.edu.hk) (M. Li).

<sup>1</sup> The two authors have the same contribution to this study.

## Nomenclature

### Symbols

$\alpha$	Transfer coefficient
$\bar{\sigma}$	Stress tensor, [N/m <sup>2</sup> ]
$\delta$	Thickness, [m]
$\eta$	Activation overpotential
$\gamma$	Pre-exponential coefficient, [A/m <sup>2</sup> ]
$J$	Species diffusion flux, [kg/m <sup>2</sup> s]
$\mu$	Viscosity, [Pa s]
$\phi_{\text{ele}}$	Electrical potential, [V]
$\phi_{\text{ion}}$	Ionic potential, [V]
$\sigma$	Electrical conductivity, [S/m]
$\bar{\sigma}$	Ionic conductivity, [S/m]
$\epsilon$	Porosity
$\zeta$	Ratio of reactive surface area to the volume, [1/m]
$c_p$	Thermal capacity, [J/kg K]
$E$	Total energy, [J/kg]
$E_{\text{act}}$	Activation energy, [J/mol]
$E_{\text{rev}}$	Reversible potential, [V]
$F$	Faraday constant, [C/mol]
$h$	Sensible enthalpy, [J/kg]
$J$	Volumetric current density, [A/m <sup>3</sup> ]
$J_0$	Exchange current density, [A/m <sup>3</sup> ]
$K$	Permeability, [m <sup>2</sup> ]
$k$	Thermal conductivity, [W/m K]
$M$	Molar mass, [kg/mol]
$p$	Pressure, [Pa]
$p_{\text{H}_2}$	Partial pressure of H <sub>2</sub> , [Pa]
$p_{\text{op}}$	Operating pressure [atm]
$R$	Ideal gas constant, [J/mol K]
$S$	Source term
$T$	Temperature, [K]
$t$	Time, [s]
$v$	Velocity, [m/s]
$X_i$	Mole fraction of species $i$
$Y_i$	Mass fraction of species $i$

### Subscripts

$i$	Species $i$
E	Electrolyte
ele	Electronic
f	Fluid
FCH	Fluid channel
ion	Ionic
s	Solid

### Abbreviations

ADL	Anode diffusion layer
AFL	Anode functional layer
CDL	Cathode diffusion layer
CFL	Cathode functional layer
DL	Diffusion layer
L	Length

FL	Functional layer
SOC	Solid oxide cell
SOEC	Solid oxide electrolysis cell
SOFC	Solid oxide fuel cell
TPB	Triple phase boundary

power with the electrolyser is the mismatch between their current–voltage ( $I - U$ ) characteristics. As the generated power exceeds the power consumption rate of the electrolyser, the excessive power is converted to waste heat that results in the low STH efficiency of the whole system. To cope with this issue, an effective strategy is to operate the power source and electrolyser near the cross-point of their steady  $I - U$  curves [14]. However, under dynamic, realistic conditions, the effectiveness of this strategy may be impaired significantly due to the difference between the transient and steady  $I - U$  characteristics of electrolyser. Thus, it is of importance to study the transient characteristics of SOEC under varying operating conditions.

The steady state  $I - U$  characteristics of solid oxide cell (SOC) – including SOEC and solid oxide fuel cell (SOFC) – at different flow field designs [15] and operating conditions [16,17] have been extensively studied in literature. By contrast, there is less information about the transient characteristics of SOC. The significant difference between the steady and transient  $I - U$  characteristics of SOC, which usually occurs as electrical undershoots or overshoots after fast load changes, has been observed in a number of experiments. Experiments in Refs. [18,19] displayed the current overshoots or undershoots of SOC after rapid changes of voltage. Experiments in Refs. [20,21] induced voltage overshoots by varying current. However the electrical undershoots have not quantitatively evaluated and physically explained due to the lack of high-fidelity, dynamic, experimental data. As a complement of experiments, the numerical simulation, in spite of the high computational cost, can provide comprehensive data to resolve the transient behaviors of SOC spatially and temporally.

With numerical simulations, a number of studies have reported the electrical overshoots or undershoots under various situations, e.g., fast changes of current [22] or voltage [23,24], sudden failures [11,25], and mode switching [9,26]. Whereas, two inconsistencies are detected in these studies. One inconsistency lies in the relaxation time of electrical overshoots or undershoots. In studies [24,27,28], the relaxation time is around 0.1 s in contrast to the hundreds of seconds reported by other studies [22,23,29,30]. While in studies [31,32], it is found that the relaxation is fast in the first 0.1 s and then slows down in the subsequent hundreds of seconds. The other inconsistency lies in the opinions on the causes of electrical overshoots or undershoots. References. [22,32] argued that the thermal inertia may be the cause, while [27,28] were prone to the gas propagation delay. The two inconsistencies imply that the transient characteristics of SOC still require further investigations. Albrecht and Braun's study [33] reported the different dynamics of fuel species from 1-D and quasi-2-D SOFC models and revealed that the spatial resolution of the numerical model probably has a strong effect on the transient simulation results. Bae et al. [28] performed a high-fidelity, 3-D transient simulation on the transient responses of SOFC upon step change of voltage with a constant time step size of 10<sup>-4</sup> s. They indicated that the time delay induced by hydrogen diffusion leads to the excessive response of current. They also pointed out that the fluctuating load may lead to pressure fluctuation which may impose stress on the electrolyte. However, due to the limited simulation time — around 3 s, they did not identify the transient behaviors of SOFC in the subsequent hundreds of seconds.

Overall, 3-D numerical simulation on SOC with high spatial and temporal resolution and sufficient simulation time is absent in the literature. Correspondingly, there is a lack of quantitative and comprehensive analysis of the transient characteristics of SOC — especially the

maturity of SOEC, e.g., thermal safety [9,10], degradation [11,12], and stability [13], especially under dynamic operating conditions. Besides, according to Ref. [14], one of the main challenges in integrating solar

electrical responses to different changes in current or voltage. To fill these research gaps in this study, we conducted 3-D simulation on SOEC with high spatial and temporal resolutions (up to  $10^{-6}$  s) in a long time span of  $10^4$  s. An adaptive time-stepping strategy was utilized to balance the computational costs of temporal resolution and simulation time. Based on the high-fidelity simulation data, we not only explained the physics of transient characteristics comprehensively but also quantified the time constants that govern the electrical responses. To the best of our knowledge, the quantification method, which is developed from the response equations of linear time-invariant systems, is firstly applied on the SOC transient studies to acquire time constants, which is also expected to be adaptable for other SOC systems with similar structures. In addition, this study will provide a solid theoretical basis for the dynamic coupling of SOEC with intermittent renewable power sources, as well as the control strategy and structure design of SOEC.

In the following, the developed numerical model and time-stepping strategy are introduced in Section 2., The detailed parameters of the numerical model are listed in Appendix A. In Section 3.1, the transient characteristics of SOEC in response to a fast voltage ramp is presented. In Section 3.2, the transient responses at different positions in SOEC are discussed. In Section 3.3, the transient current responses to voltage ramps with different ramp magnitudes are compared. In Section 3.4, the transient characteristics of SOEC under different ramp rates of voltage are presented. In Section 3.5, the time constants that govern the electrical responses of SOEC are quantified. Conclusions are summarized in Section 4.

## 2. Numerical modeling

SOC is an electrochemical device that can operate in two modes, namely SOEC and SOFC. Due to the similar electrochemical principles, SOEC and SOFC can share one numerical model of SOC with little modifications when switching modes. To investigate the transient characteristics of SOEC, a planar cathode-supporting SOEC is considered in this study. The planar SOEC can be simplified into a single-channel model, which has been proved to be effective in representing the overall performance of a planar cell with a low computational cost [34]. In this section, a 3-D single-channel model of SOC is developed in Ansys Fluent based on the 1-D button-cell model provided by Njodzefon et al. [35]. Then, an adaptive time-stepping strategy is proposed to balance the computational costs of temporal resolution and simulation time. The species diffusion model, electrochemical model, source terms, boundary conditions, and the time-stepping algorithm mentioned in this section are written into Ansys Fluent through User-Defined Function (UDF).

### 2.1. Geometry

As shown in Fig. 1, the single-channel model of SOEC is composed of an anode diffusion layer (ADL), an anode functional layer (AFL), a solid oxide electrolyte, a cathode functional layer (CFL), a cathode diffusion layer (CDL), two fluid channels (one for  $H_2$  and  $H_2O$ , the other for  $O_2$  and  $N_2$ ), and two interconnects with ribs. The fluid channels are prolonged for sufficient mixing of gases [36]. Besides, each layer of the SOEC is modeled as a continuum so that Finite Volume Method (FVM) can be applied to solve the model numerically. The mesh scheme is also displayed in Fig. 1. The total number of meshes is about 1,090,000, which is able to achieve grid independence for our studied cases. Detailed Geometric parameters of the SOEC are presented in Table 1, while the boundary conditions of the numerical model are presented in Table 2.

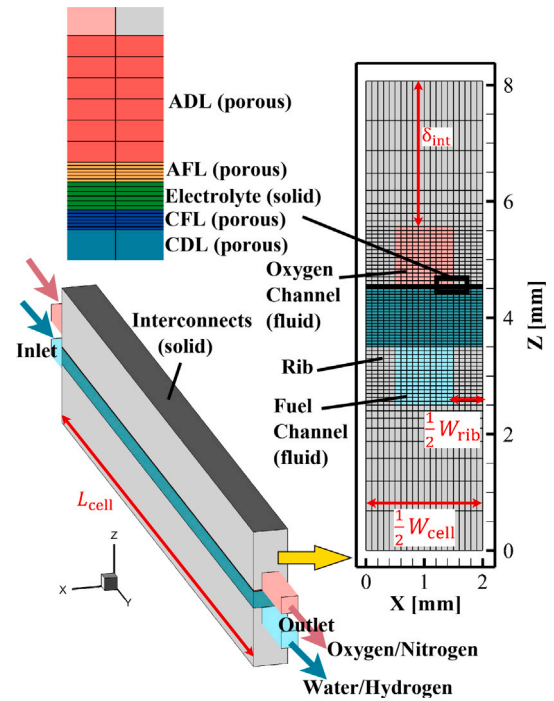


Fig. 1. The geometry and mesh scheme of SOEC used in the CFD simulation.

Table 1

Geometric parameters of the SOC [34,35] for simulation. The naming rule of ‘cathode’ (fuel electrode) and ‘anode’ (air electrode) used here is according to the SOEC mode.

Geometric parameters	Value [m]	Ref.
Height of fluid channel, $H_{FCH}$	$1 \times 10^{-3}$	
Width of fluid channel, $W_{FCH}$	$1 \times 10^{-3}$	
Height of rib, $H_{rib}$	$1 \times 10^{-3}$	[34]
Width of rib, $W_{rib}$	$1 \times 10^{-3}$	[34]
Length of cell, $L_{cell}$	$1 \times 10^{-1}$	
Width of cell, $W_{cell}$	$2 \times 10^{-3}$	
Thickness of interconnect, $\delta_{int}$	$2.5 \times 10^{-3}$	[34]
Thickness of ADL, $\delta_{ADL}$	$4.5 \times 10^{-5}$	[35]
Thickness of AFL, $\delta_{AFL}$	$7 \times 10^{-6}$	[35]
Thickness of electrolyte, $\delta_E$	$1 \times 10^{-5}$	[35]
Thickness of CFL, $\delta_{CFL}$	$7 \times 10^{-6}$	[35]
Thickness of CDL, $\delta_{CDL}$	$1 \times 10^{-3}$	[35]

### 2.2. Governing equations

Under SOEC mode, the SOC consumes electricity and high-temperature steam to produce hydrogen and oxygen. The voltage applied on the interconnects forces the directional migration of electrons in the electron-conducting layers — interconnects, ADL, AFL, CDL, and CFL. High-temperature steam flows through the fuel channel, penetrates into the porous CDL, and reaches CFL where electrochemical reactions split the steam into hydrogen and oxygen ion. Then, only oxygen ion is allowed to cross the solid electrolyte and reaches the AFL where oxygen is generated via electrochemical reactions. Finally, hydrogen and oxygen are released to the fuel channel and oxygen channel, respectively. SOFC mode is the reverse mode of SOEC — consuming hydrogen and oxygen to produce water and generate voltage.

The governing equations and source terms of the SOEC model are shown in Table 3 and Table 4, respectively. The electronic/ionic, heat, and mass transfer phenomena are fully coupled. The transient terms are neglected in the conservation equations of electronic charge and ionic charge since the time constants of ionic and electronic charge transfer are much smaller than those of the heat and mass transfer processes [36], and also smaller than the smallest time step size of

**Table 2**  
Boundary conditions for the CFD simulation. The operating pressure is  $p_0 = 1$  atm.

	Inlet	Outlet	$x = 0$ , $x/W_{\text{cell}} = 1$	$z = 0$	$z/\delta_{\text{cell}} = 1$	Other surfaces
Momentum	$v = 8.33$ [m/s] <sup>a</sup>	$p_{\text{gauge}} = 0$	Zero flux	N.A.	N.A.	$v = 0$
Thermal	$T = 1123.15$ [K]	N.A.	Zero flux	Zero flux	Zero flux	Zero flux
Species	$X_{\text{H}_2\text{O}} = 0.5$ , $X_{\text{H}_2} = 0.5$ , $X_{\text{O}_2} = 0.2$ , $X_{\text{N}_2} = 0.8$	N.A.	Zero flux	N.A.	N.A.	Zero flux
Electrical	N.A.	N.A.	Zero flux	$\phi_{\text{ele}} = 0$	$\phi_{\text{ele}} = f(t)^b$	Zero flux

N.A. means 'not applicable'.

<sup>a</sup>Under the specified velocity and species composition, the utilization of  $\text{H}_2\text{O}$  approximates 40% when  $i = -1.7$  A/cm<sup>2</sup>.

<sup>b</sup> $\phi_{\text{ele}}$  linearly ramps from 1.2 V to a specified voltage in a specified ramp time and finally maintains at the specified voltage.

**Table 3**  
Governing equations of SOEC [16,35,37,38].

Governing equations	
<i>Fluid channels</i>	
Continuity	$\frac{\partial \rho}{\partial t} + \nabla \cdot (\rho \vec{v}) = 0$
Momentum <sup>a</sup>	$\frac{\partial (\rho \vec{v})}{\partial t} + \nabla \cdot (\rho \vec{v} \vec{v}) = -\nabla p + \nabla \cdot (\vec{\tau})$
Species	$\frac{\partial}{\partial t} (\rho Y_i) + \nabla \cdot (\rho \vec{v} Y_i) + \nabla \cdot \vec{J}_i = 0$
Energy <sup>b</sup>	$\frac{\partial}{\partial t} (\rho E) + \nabla \cdot (\vec{v}(\rho E + p)) = \nabla \cdot (k \nabla T - \sum_i h_i \vec{J}_i)$
State function	$\rho = \frac{pM}{RT}$ (ideal gas)
<i>Porous media (ADL, AFL, CFL, CDL)</i>	
Continuity	$\frac{\partial (\epsilon \rho)}{\partial t} + \nabla \cdot (\rho \vec{v}) = S_m$
Momentum <sup>a,c</sup>	$\frac{\partial (\rho \vec{v})}{\partial t} + \nabla \cdot (\rho \vec{v} \vec{v}) = -\nabla p + \nabla \cdot (\vec{\tau}) - \frac{\mu}{K} \vec{v}$
Species	$\frac{\partial}{\partial t} (\epsilon \rho Y_i) + \nabla \cdot (\rho \vec{v} Y_i) + \nabla \cdot \vec{J}_i = S_i$
Energy <sup>b</sup>	$\frac{\partial}{\partial t} (\epsilon \rho_t E_t + (1 - \epsilon) \rho_s E_s) + \nabla \cdot (\vec{v}(\rho_t E_t + p)) = \nabla \cdot [(\epsilon k_t + (1 - \epsilon) k_s) \nabla T - (\sum_i h_i \vec{J}_i)] + S_h$
State function	$\rho = \frac{pM}{RT}$ (ideal gas)
Electronic charge	$\nabla \cdot (\sigma \nabla \phi_{\text{ele}}) + S_{\text{ele}} = 0$
Ionic charge	$\nabla \cdot (\tilde{\sigma} \nabla \phi_{\text{ion}}) + S_{\text{ion}} = 0$
<i>Solid electrolyte</i>	
Ionic charge	$\nabla \cdot (\tilde{\sigma} \nabla \phi_{\text{ion}}) = 0$
Energy <sup>b</sup>	$\frac{\partial}{\partial t} (\rho h) = \nabla \cdot (k \nabla T) + S_h$
<i>Interconnects</i>	
Electronic charge	$\nabla \cdot (\sigma \nabla \phi_{\text{ele}}) + S_{\text{ele}} = 0$
Energy <sup>b</sup>	$\frac{\partial}{\partial t} (\rho h) = \nabla \cdot (k \nabla T) + S_h$

<sup>a</sup>Stress tensor:  $\vec{\tau} = \mu \left[ (\nabla \vec{v} + \nabla \vec{v}^T) - \frac{2}{3} \nabla \cdot \vec{v} \right]$ .

<sup>b</sup>Total energy:  $E = \sum_i Y_i h_i$ ; sensible enthalpy:  $h = \int_{298.15\text{K}}^T c_p dT$ .

<sup>c</sup>The effects of porous media are modeled based on superficial velocity. The last term represents the viscous forces imposed by the pore walls on the fluid.  $K$  is permeability.

this study. The material parameters used in the governing equations are listed in Table A.1.

### 2.2.1. Species diffusion model

Fick's law is applied to model the mass diffusion flux  $\vec{J}$  in the species conservation equations. In the fluid channels:

$$\vec{J}_i = -\rho D_i \nabla Y_i, \quad (1)$$

where  $Y_i$  is the mass fraction of species  $i$ .  $D_i$  is the binary diffusion coefficient of species  $i$  in the fluid channel, which is determined from the Chapman–Enskog theory [35,41]. For the mass diffusion flux in porous media, the extended Fick's model is adopted:

$$\vec{J}_i = -\rho D_i^{\text{eff}} \nabla Y_i \quad (2)$$

where  $D_i^{\text{eff}}$  is the effective molecular diffusion coefficient, the calculation procedure of which can be found in a series of studies [35,42,43].

**Table 4**  
Source terms.

Source terms	Unit
$S_m = S_{\text{H}_2\text{O}} + S_{\text{H}_2} + S_{\text{O}_2}$	[kg m <sup>-3</sup> s <sup>-1</sup> ]
$S_{\text{H}_2\text{O}} = \begin{cases} \frac{M_{\text{H}_2\text{O}}}{2F} J_{\text{cat}} & \text{CFL} \\ 0 & \text{AFL, ADL, CDL} \end{cases}$	[kg m <sup>-3</sup> s <sup>-1</sup> ]
$S_{\text{H}_2} = \begin{cases} -\frac{M_{\text{H}_2}}{2F} J_{\text{cat}} & \text{CFL} \\ 0 & \text{AFL, ADL, CDL} \end{cases}$	[kg m <sup>-3</sup> s <sup>-1</sup> ]
$S_{\text{O}_2} = \begin{cases} -\frac{M_{\text{O}_2}}{4F} J_{\text{an}} & \text{AFL} \\ 0 & \text{CFL, CDL, ADL} \end{cases}$	[kg m <sup>-3</sup> s <sup>-1</sup> ]
$S_{\text{ele}} = \begin{cases} J_{\text{an}} & \text{AFL} \\ -J_{\text{cat}} & \text{CFL} \\ 0 & \text{CDL, ADL} \end{cases}$	[A m <sup>-3</sup> ]
$S_{\text{ion}} = \begin{cases} -J_{\text{an}} & \text{AFL} \\ J_{\text{cat}} & \text{CFL} \\ 0 & \text{CDL, ADL} \end{cases}$	[A m <sup>-3</sup> ]
$S_h = \begin{cases} S_{\text{ohm}}^{\text{ion}} & \text{Electrolyte} \\ S_{\text{ohm}}^{\text{ele}} & \text{CDL, ADL, Interconnect} \\ S_{\text{ohm}}^{\text{ele}} + S_{\text{ohm}}^{\text{ion}} + S_{\text{irrev}} + S_{\text{rev}} & \text{CFL, AFL} \end{cases}$	[W m <sup>-3</sup> ]
$S_{\text{ohm}}^{\text{ion}} = \tilde{\sigma} (\nabla \phi_{\text{ion}})^2$	[W m <sup>-3</sup> ]
$S_{\text{ohm}}^{\text{ele}} = \sigma (\nabla \phi_{\text{ele}})^2$	[W m <sup>-3</sup> ]
$S_{\text{irrev}} + S_{\text{rev}} = \begin{cases} J_{\text{cat}} \eta_{\text{cat}} + \frac{J_{\text{cat}} T (\frac{1}{2} \Delta S_f)}{2F} & \text{CFL} \\ -J_{\text{an}} \eta_{\text{an}} + \frac{J_{\text{an}} T (\frac{1}{2} \Delta S_f)}{2F} & \text{AFL} \end{cases}$	[W m <sup>-3</sup> ]

<sup>a</sup>The reversible heat source is negative in SOEC mode and positive in SOFC mode.  $\Delta S_f$  is the non-standard entropy of formation for the overall reaction:  $\text{H}_2 + 0.5\text{O}_2 \rightarrow \text{H}_2\text{O}$ . It is a common treatment to equally assign  $\Delta S_f$  to AFL and CFL [39].  $\Delta S_f$  is fitted from NIST database [40] at  $p = 1$  atm,  $T = 400$  K  $\sim$  1300 K:  $\Delta S_f = -6.578 \times 10^{-9} \times T^3 + 2.650 \times 10^{-5} \times T^2 - 0.0395 \times T - 35.79$ .

### 2.2.2. Electrochemical model

FL contains gas phase, ionic conducting phase, and electronic conducting phase. At the triple-phase boundary (TPB), electrochemical reactions take place. In the AFL (air electrode), the electrochemical reaction involved in SOEC mode is,



And in the CFL (fuel electrode), the electrochemical reaction is,



To simulate the electrochemical reactions, the Butler–Volmer (B–V) equation, which is deduced from single-step and single-electron-transfer reactions, is widely adopted to model the multi-electron and multi-step reactions in the SOC [37]. It has shown sufficient accuracy in the prediction of the electrochemical characteristics of SOC [16,44]. The B–V equation [37] adopted in this study is,

$$J_{\text{cat}} = \zeta_{\text{cat}} J_{0,\text{cat}} \left[ \exp \left( \alpha_{\text{cat}} \frac{n_e F \eta_{\text{cat}}}{RT} \right) - \exp \left( - (1 - \alpha_{\text{cat}}) \frac{n_e F \eta_{\text{cat}}}{RT} \right) \right] \quad (5)$$

$$J_{\text{an}} = \zeta_{\text{an}} J_{0,\text{an}} \left[ \exp \left( \alpha_{\text{an}} \frac{n_e F \eta_{\text{an}}}{RT} \right) - \exp \left( - (1 - \alpha_{\text{an}}) \frac{n_e F \eta_{\text{an}}}{RT} \right) \right] \quad (6)$$

where,  $F$  is the Faraday constant ( $F = 96485.3 \text{ C/mol}$ ),  $R$  is the universal gas constant ( $R = 8.314 \text{ J/K.mol}$ ),  $n_e$  is the number of electrons produced or consumed by the reaction ( $n_e = 2$ ),  $\alpha$  is the transfer coefficient,  $\zeta$  represents the ratio of reactive surface area to the volume of FL. The exchange current density  $J_0$  [ $\text{A/m}^2$ ] is modeled by the following semi-empirical equations [37],

$$J_{0,\text{cat}} = \gamma_{\text{cat}} \left( p_{\text{H}_2,\text{cat}}^{\text{TPB}} \right)^a \left( p_{\text{H}_2\text{O},\text{cat}}^{\text{TPB}} \right)^b \exp \left( -\frac{E_{\text{act,cat}}}{RT} \right) \quad (7)$$

$$J_{0,\text{an}} = \gamma_{\text{an}} \left( p_{\text{O}_2,\text{an}}^{\text{TPB}} \right)^m \exp \left( -\frac{E_{\text{act,an}}}{RT} \right) \quad (8)$$

where,  $a$ ,  $b$ , and  $m$  are concentration-dependent coefficients,  $\gamma$  is an adjustable parameter,  $E_{\text{act}}$  is the activation energy,  $p_{\text{H}_2,\text{cat}}^{\text{TPB}}$  denotes the partial pressure of  $\text{H}_2$  at the TPB of cathode (CFL),  $\eta$  is the activation overpotential defined as [44],

$$\eta_{\text{cat}} = \phi_{\text{ele}} - \phi_{\text{ion}} \quad (9)$$

$$\eta_{\text{an}} = \phi_{\text{ele}} - \phi_{\text{ion}} - E_{\text{rev}} \quad (10)$$

The reversible electrical potential  $E_{\text{rev}}$  is,

$$E_{\text{rev}} = \left| \frac{\Delta G_f(T, p)}{2F} \right| + \frac{RT}{2F} \ln \left[ \left( \frac{p_{\text{H}_2}}{p_{\text{H}_2\text{O}}} \right) \left( \frac{p_{\text{O}_2}}{p} \right)^{0.5} \right] \quad (11)$$

where,  $\Delta G_f(T, p)$  is the non-standard Gibbs free energy of formation, which can be obtained from the NIST database [40]. At  $p_0 = 1 \text{ atm}$ , the first term on the right hand side of Eq. (11) can be expressed as a fitted function of temperature:

$$\left| \frac{\Delta G_f(T, p_0)}{2F} \right| = -2.415 \times 10^{-8} \times T^2 - 0.00023562 \times T + 1.2598 \quad (12)$$

The parameters required for the electrochemical model are listed in Table A.2.

### 2.3. Calculation procedure

The numerical model is solved using Ansys Fluent R18.1. PISO scheme is adopted for pressure-velocity coupling. At  $t = 0$ , the transient simulation is initialized with the steady-state solution under  $U = 1.2 \text{ V}$ . Then, for a given ramp time ( $\Delta t_{\text{ramp}} = t_{\text{ramp}} - 0$ ), the voltage changes linearly from  $1.2 \text{ V}$  to a specified voltage in  $0 < t \leq t_{\text{ramp}}$  and maintains at the specified voltage during  $t_{\text{ramp}} < t \leq 10^4 \text{ s}$ . The transient simulation stops until a new steady state has been reached or  $t = 10000 \text{ s}$ . The convergence criteria are: residual of energy is less than  $10^{-12}$ , residual of  $Y_{\text{H}_2}$  is less than  $10^{-6}$ , and residual of  $\phi_{\text{ele}}$  is less than  $10^{-9}$ .

The investigated  $\Delta t_{\text{ramp}}$  ranges from  $10^{-5} \text{ s}$  to  $10^3 \text{ s}$ . To resolve such a wide range of time scale, it would be computationally expensive if using a constant time-stepping strategy. For example, a simulation case of  $10^4 \text{ s}$  with a constant time-step size of  $10^{-5} \text{ s}$  requires  $10^9$  time steps to compute. Thus, an adaptive time-stepping strategy is developed to balance the temporal resolution and the computational cost. At the beginning of voltage change, the voltage ramp is resolved by at least 10 time steps. After the voltage ramp, the adaptive time-stepping size  $\Delta t$  for the next time step  $t^{n+1}$  is calculated based on the  $T_{\text{ave}}$  (averaged over the whole cell) and  $Y_{\text{H}_2,\text{ave}}$  (averaged over the fuel electrode) at the current time step  $t^n$  and the previous time step  $t^{n-1}$ . The strategy aims to control the variation of temperature at around  $0.01 \text{ K/step}$  or that of  $\text{H}_2$  mass fraction at around  $0.2\%/\text{step}$ . The specific method is expressed in Eq. (13). With the adaptive time-stepping strategy, the simulation with a time scale from  $10^{-6} \text{ s}$  to  $10^4 \text{ s}$  can be completed within around 2000 time steps.

$$\Delta t^{n+1} = \begin{cases} \frac{\Delta t_{\text{ramp}}}{10} & 0 \leq t < t_{\text{ramp}} \\ \Delta t^n \cdot \text{MIN} \left( \frac{0.01}{|T_{\text{ave}}^{n-1} - T_{\text{ave}}^n|}, \frac{0.002}{|Y_{\text{H}_2,\text{ave}}^{n-1} - Y_{\text{H}_2,\text{ave}}^n|} \right) & t_{\text{ramp}} \leq t < 10^4 \end{cases} \quad (13)$$

### 2.4. Validation

The validation of the developed numerical model (including both the SOFC and SOEC modes) is performed by comparing with the experimental data from the study of Njodzefon et al. [35]. The experiment was performed on a square button cell with  $1 \text{ cm}^2$  active area, and the data were measured under constant temperature conditions. To be consistent with the experimental setup, the geometry of the numerical model used for validation is the same button cell as used in the experiment. The single-channel model used in subsequent analysis and the button-cell model used for validation are identical except for the size of active area and boundary conditions. Besides, the operating conditions of the validation cases are consistent with the experiment. More specifically, the constant-temperature boundary condition is applied on the top and bottom of the button cell, the operating pressure is at  $1 \text{ atm}$ , the gas flow rates for both electrodes are  $250 \text{ sccm}$ , and the oxidant gas is air ( $20\% \text{ O}_2$ ,  $80\% \text{ N}_2$ ). The composition of the  $\text{H}_2\text{O}-\text{H}_2$  mixture for the fuel electrode, voltage, and temperature are the control variables in the validation cases.

The simulation result and the experimental data are compared in Fig. 2. The negative current density indicates the cell is operating under SOEC mode, while the positive current density indicates the SOFC mode. Under the SOEC mode, less voltage is required for electrolysis when higher  $\text{H}_2\text{O}$  concentration or gas temperature is applied, since the increase of reactant concentration or temperature can decrease the reversible potential. In addition, the high temperature is also beneficial in reducing activation loss. The shortage of  $\text{H}_2\text{O}$  at high current magnitude, such as the case with  $X_{\text{H}_2\text{O}} = 30\%$  and  $i = -2.2 \text{ A/cm}^2$ , will lead to a significant increase of voltage. For validation purpose, the simulation results agree well with the experimental data for cases with current density ranging from  $-2 \text{ A/cm}^2$  to  $1 \text{ A/cm}^2$ , cell temperature ranging from  $800 \text{ }^\circ\text{C}$  to  $850 \text{ }^\circ\text{C}$ , and the molar fraction of  $\text{H}_2\text{O}$  at the inlet ranging from  $30\%$  to  $70\%$ . According to the analysis in Ref. [35], the disagreement between simulation and experimental data, especially for the SOFC mode at high current magnitude, may be caused by the temperature difference between FL and the temperature measuring point during the experiment.

## 3. Results and discussion

In this section, transient simulation is conducted with the 3-D single-channel SOEC model. We adopt the case with a linear voltage ramp from  $1.2 \text{ V}$  to  $1.0 \text{ V}$  in  $10^{-5} \text{ s}$  as the base case to analyze the transient processes in SOEC. with regard to the base case, not only the electrical, gaseous, and thermal responses but also the spatial non-uniformity of dynamic responses are analyzed. The analysis is then extended to the cases with different voltage ramp magnitudes and ramp rates. Furthermore, the time constants that govern the electrical responses of SOEC are quantified.

### 3.1. Responses to a linear voltage ramp

At  $t = 0 \text{ s}$ , the base case starts from the steady-state solution of the SOEC with voltage of  $1.2 \text{ V}$ . Then, the voltage ramps down linearly from  $1.2 \text{ V}$  to  $1.0 \text{ V}$  in  $10^{-5} \text{ s}$ . For  $t > 10^{-5} \text{ s}$ , the voltage is held at  $1.0 \text{ V}$  until  $10^4 \text{ s}$ . Fig. 3 demonstrates the variations of current density magnitude, mole fraction of  $\text{H}_2\text{O}$ , and average temperature of FL from one steady state to another steady state ( $t = t_{\text{steady}} = 10^3 \text{ s}$ ) for the base case. For comparison, the steady-state  $I - U$  curve that shows the relationship between current and voltage for the base case is also plotted. Besides, the three marked time points indicate the time at the end of the voltage ramp ( $t_{\text{ramp}}$ ), at the end of the fast relaxation of current ( $t_{\text{quasi}}$ ), and at the new steady state ( $t_{\text{steady}}$ ), respectively.

In Fig. 3, an overshoot of  $\text{H}_2\text{O}$  mole fraction is observed and its relaxation occurs from  $10^1 \text{ s}$  to  $10^3 \text{ s}$ , which is consistent with Nerat's

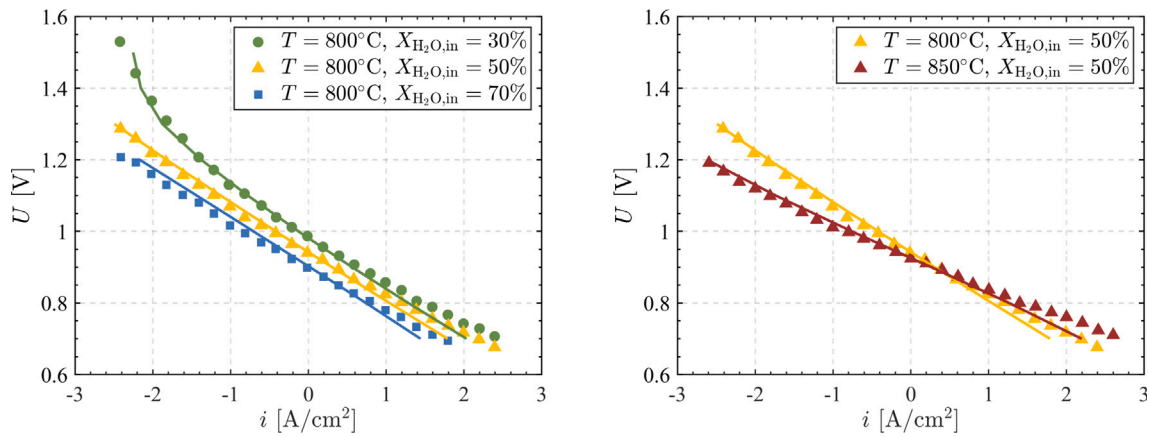


Fig. 2. Voltage ( $U$ ) with respect to current density ( $i$ ) of our simulation results and the experimental data in [35]. Solid lines represent simulation data while dots denote experimental data.

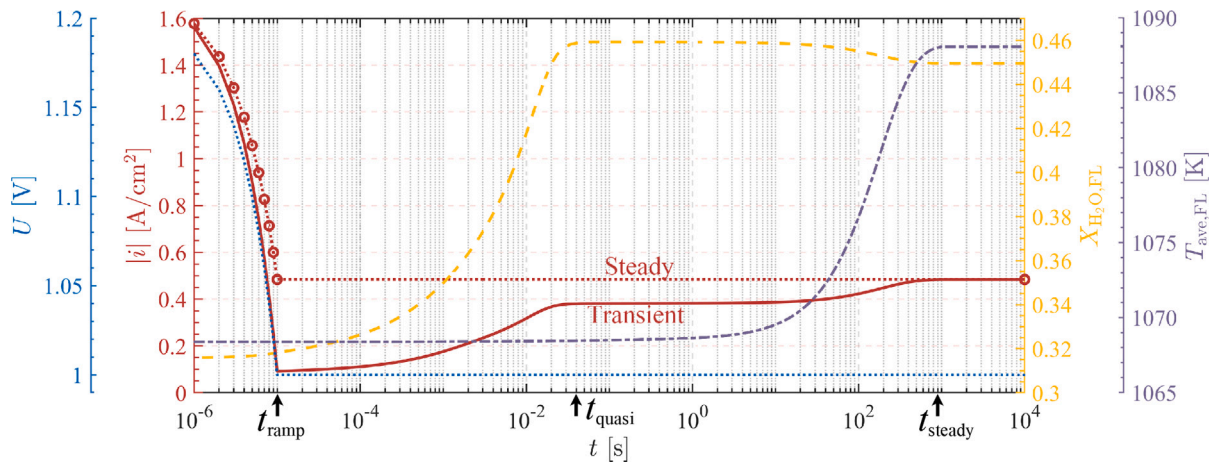


Fig. 3. Voltage ( $U$ ), current density magnitude ( $|i|$ ), mole fraction of  $H_2O$  in FL ( $X_{H_2O,FL}$ ), and average temperature in FL ( $T_{ave,FL}$ ) versus time ( $t$ ), which represents the electrical, molar, and thermal responses of SOEC to a linear voltage ramp from 1.2V to 1.0V in  $10^{-5}$  s. The solid red line indicates the transient response of current density magnitude, and the dotted red line with circle marks indicates the steady-state current density magnitude under the given voltage. (A video clip is provided in the supplementary material to illustrate the corresponding transient responses.)

study [27]. More importantly, the response of current density magnitude undergoes a significant undershoot due to the voltage ramp. At the end of the voltage ramp ( $t = t_{ramp}$ ), the current density magnitude decreases to the minimum — around  $0.1 \text{ A/cm}^2$ , which is far lower than the value  $0.48 \text{ A/cm}^2$  at  $t = t_{steady}$ . After the voltage ramp, the current density magnitude undergoes a fast relaxation from  $10^{-5}$  s to  $10^{-2}$  s before the quasi-steady state ( $t_{ramp} < t < t_{quasi}$ ), and a slow relaxation from  $10^1$  s to  $10^3$  s before the final steady state ( $t_{quasi} < t < t_{steady}$ ). In practice, the undershoot current magnitude will cause under-production of hydrogen. Besides, the rapid variation of voltage leads to a significant deviation of the transient  $I-U$  characteristic from the steady-state one, as evidenced by the two entirely different red curves in Fig. 3. In addition, the deviation tends to last for a long time — around 500 s in the investigated case. For a solar-SOEC integrated system that relies on coupling the steady  $I-U$  characteristics of the power source and the electrolyser to achieve maximum STH efficiency [14], the deviated transient  $I-U$  characteristic of electrolyser will certainly lead to the under-performance of the whole system and the curtailment of solar power production.

To identify the fundamental causes of current undershoot, it is necessary to find out the independent variables that determine the current density. According to the electrochemical model (Section 2.2.2), the current density that reflects the electrochemical reaction rate of SOEC is a function of several variables in FL, i.e., the partial pressures of the reactant ( $p_{H_2O}$ ) and products ( $p_{H_2}$ ,  $p_{O_2}$ ), absolute pressure  $p_{abs}$ ,

temperature  $T$ , electrical potential  $\phi_{ele}$ , and ionic potential  $\phi_{ion}$ , which can be expressed as:

$$i = f(T, p_{H_2}, p_{H_2O}, p_{O_2}, p_{abs}, \phi_{ele}, \phi_{ion}) \quad (14)$$

Considering the pressure variation within the SOEC is at the order of 100 Pa, which is small compared to the absolute pressure  $\sim 10^5$  Pa, the pressure dependence can be neglected in Eq. (14). Then, the partial pressure can be replaced with mole fraction to obtain Eq. (15),

$$i \approx f(T, X_{H_2O}, X_{H_2}, X_{O_2}, \phi_{ele}, \phi_{ion}) \quad (15)$$

where the variation rates of  $X_{H_2O}$ ,  $X_{H_2}$ , and  $X_{O_2}$  represent mass transfer rate, the variation rate of  $T$  represents heat transfer rate, and the variation rates of  $\phi_{ele}$  and  $\phi_{ion}$  represent the electronic charge and ionic charge transfer rates. These transfer rates are compared in Fig. 3 with a logarithmic coordinate and a wide timescale from  $10^{-6}$  s to  $10^4$  s.

In SOEC, the electronic charge and ionic charge transfers are much faster than the mass transfer and heat transfer [36]. Hence, as the voltage ramp finishes at  $10^{-5}$  s ( $t = t_{ramp}$ ), the mole fraction of  $H_2O$  and temperature are almost unchanged when compared to their initial values, while the current density comes to a new state with  $i|_{t=t_{ramp}} = 0.092 \text{ A/cm}^2$ . The value of  $i|_{t=t_{ramp}}$  can be approximated as,

$$i|_{t=t_{ramp}} \approx f(T|_{t=0}, X_{H_2O}|_{t=0}, X_{H_2}|_{t=0}, X_{O_2}|_{t=0}, \phi_{ele}|_{t=t_{ramp}}, \phi_{ion}|_{t=t_{ramp}}) = 0.087 \quad (16)$$

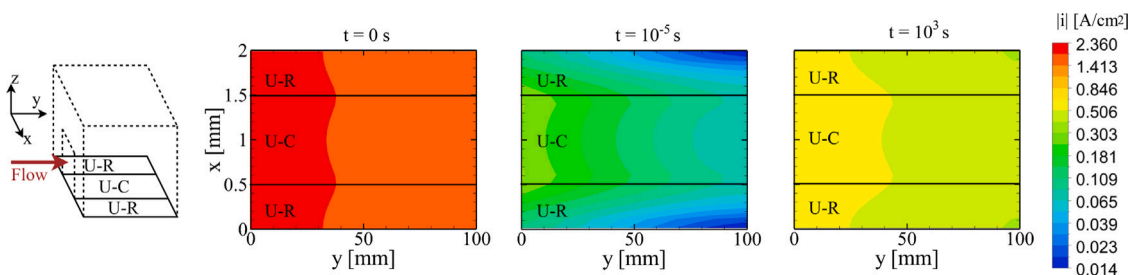


Fig. 4. Distributions of current density magnitude in AFL at the initial state ( $t = 0$  s), at the end of voltage ramp ( $t = t_{\text{ramp}} = 10^{-5}$  s), and at the final steady state ( $t = t_{\text{steady}} = 10^3$  s). U-C indicates the under-channel region and U-R indicates the under-rib regions. The color map is arranged in logarithmic scale. The aspect ratios of layers have been adjusted.

where  $f(\cdot)$  means calculating the current by the numerical model with specified inputs. Apparently, both  $T|_{t=0}$  and  $X_{\text{H}_2\text{O}}|_{t=0}$  are lower than  $T|_{t=t_{\text{steady}}}$  and  $X_{\text{H}_2\text{O}}|_{t=t_{\text{steady}}}$ . And either the low temperature or the lack of reactant weakens the electrochemical reaction rate and the current density magnitude. As a result, the current density magnitude at  $t = 0$  is lower than that at  $t = t_{\text{steady}}$ . While the low current density magnitude also means a low consumption rate of  $\text{H}_2\text{O}$  for SOEC. Consequently, accumulation of  $\text{H}_2\text{O}$  is observed in FL from  $10^{-5}$  to  $10^{-2}$  s. Correspondingly, the rise of  $\text{H}_2\text{O}$  (reactant) concentration contributes to the increase of current density magnitude from  $10^{-5}$  s to  $10^{-2}$  s, i.e., the fast relaxation period. As for the heat transfer, it is much slower than the mass transfer in SOEC [36]. Thus, as the species concentrations (e.g.,  $\text{H}_2\text{O}$ ) in FL and the current develop to the quasi-steady state ( $t = t_{\text{quasi}}$ ), the variation of temperature in the FL is still insignificant. At  $t = t_{\text{quasi}}$ , the current density is  $0.380 \text{ A/cm}^2$ , which can also be approximated as,

$$i|_{t=t_{\text{quasi}}} \approx f\left(T|_{t=0}, X_{\text{H}_2\text{O}}|_{t=t_{\text{quasi}}}, X_{\text{H}_2}|_{t=t_{\text{quasi}}}, X_{\text{O}_2}|_{t=t_{\text{quasi}}}, \phi_{\text{ele}}|_{t=t_{\text{quasi}}}, \phi_{\text{ion}}|_{t=t_{\text{quasi}}}\right) = 0.381 \quad (17)$$

The SOEC that operates under the investigated voltage is endothermic. When  $t < t_{\text{steady}}$ , the undershoot of current magnitude, i.e. the excessively low electrochemical reaction rate weakens the endothermic effect and hence leads to heat accumulation and temperature rise in FL. Correspondingly, the increase of temperature can improve the electrochemical reaction rate and result in an increase of current density magnitude from  $10^1$  s to  $10^3$  s, i.e., the slow relaxation period. But the increase of current density would accelerate the consumption of the reactant  $\text{H}_2\text{O}$ . So, the mole fraction of  $\text{H}_2\text{O}$  decreases from  $10^1$  s to  $10^3$  s. In short, the undershoot of current magnitude is caused by the different response time: electrical response time  $<$  molar response time  $<$  thermal response time. With regards to the relaxation of current magnitude, the fast relaxation is governed by mass transfer, while the slow relaxation is governed by heat transfer. The overshoot of  $\text{H}_2\text{O}$  concentration is due to the faster transfer rate of mass than heat.

### 3.2. Transient characteristics of SOEC at different positions

To investigate the spatial differences of dynamic responses of the base case, the current density data at different time steps in AFL are extracted and averaged over the  $z$ -direction. Fig. 4 shows the non-uniform distributions of current density magnitude in the FL of SOEC. In contrast to the initial and final steady states, at the end of voltage ramp ( $t = 10^{-5}$  s), a more significant gradient of current density exists not only along the channel but also between the under-channel and under-rib regions. The non-uniformity of current density implies that the intensities of electrical responses are affected by cell structure, such as the rib size and the length of the cell.

To further clarify the impacts of cell structure, the current density data under the center of channel and the center of rib are extracted. Fig. 5(a) compares the variations of current density in the stream-wise direction, as well as between the under-channel and under-rib regions.

It can be observed that the electrochemical reaction intensity under the rib tends to be weaker than that under the channel, as evidenced by the lower current magnitude in the under-rib region. An explanation is that the ribs hinder the diffusion of reactants from the channel to FL and the diffusion of products from FL to channel. Another observation from Fig. 5(a) is that the position closer to the inlet has larger current magnitude and stronger response intensity.

In addition, it is noticed that all the curves in Fig. 5(a) experience two stages of upward retracement after undershoot. As discussed in Section 3.1, the two stages of current retracement are related to the slow rises of reactant concentration and temperature, respectively. Based on the two stages of current retracement, we further decompose the undershoot of current magnitude into two parts. One part is related to the slow mass transfer, and the other part is related to the slow heat transfer. These two parts of undershoots are normalized according to Eqs. (18) and (19) to provide a quantitative understanding on the electrical responses at each  $y$  coordinate. Subscript  $y$  is omitted for simplicity in Eqs. (18) and (19).

$$\Delta i_{\text{mass}}^* = \frac{|i|_{t=t_{\text{ramp}}} - i|_{t=t_{\text{quasi}}}|}{|i|_{t=0} - i|_{t=t_{\text{steady}}}|} \quad (18)$$

$$\Delta i_{\text{heat}}^* = \frac{|i|_{t=t_{\text{quasi}}} - i|_{t=t_{\text{steady}}}|}{|i|_{t=0} - i|_{t=t_{\text{steady}}}|} \quad (19)$$

Fig. 5(b) compares the normalized undershoots of current density magnitude under the rib and under the channel at different  $y$  coordinates. In general, the current undershoot induced by mass-transfer lag contributes to around 50%–80% of the total undershoot. In the aspect of stream-wise differences, the magnitude of the undershoot, either induced by mass-transfer lag or by heat-transfer lag, becomes larger as the position being closer to the outlet ( $y/L = 1$ ). This can be explained by the time lag of advection, which means the variable fields (e.g. species concentration and temperature) in upstream affect the ones in downstream and the downstream requires time to ‘feel’ the changes that have happened in the upstream. Thus, at the position closer to the outlet, the advection lag is more significant and causes a more severe normalized undershoot. The quantitative analysis of advection lag will be discussed in Section 3.5.

With regard to the comparison between under-channel and under-rib cases, the larger undershoot at the under-rib region is mainly contributed by the larger mass-transfer lag under the rib as shown in Fig. 5(b). More specifically, the under-rib undershoot caused by mass-transfer lag is 20%–30% higher than the under-channel one and is almost independent of the stream-wise position, which implies that the hindering effect of the rib on the mass transfer is strong and consistent in the stream-wise direction.

### 3.3. Responses to voltage ramps with different ramp magnitudes

To have a more general view of the transient responses of SOEC, simulation cases with different ramp magnitudes are conducted. Fig. 6 compares the responses of current magnitude to voltage ramps with four different ramp magnitudes, namely the ramps from 1.2 V to 1.0 V,

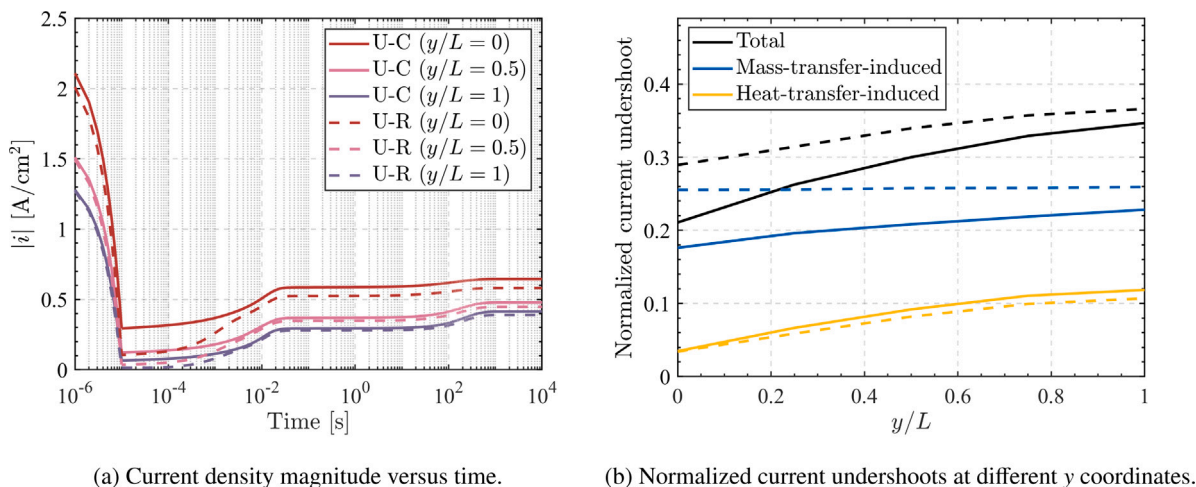


Fig. 5. Comparisons on electrical responses at under-channel (U-C) and under-rib (U-R) positions and at different y coordinates (stream-wise direction). Solid lines represent U-C data, dotted lines represent U-R data.

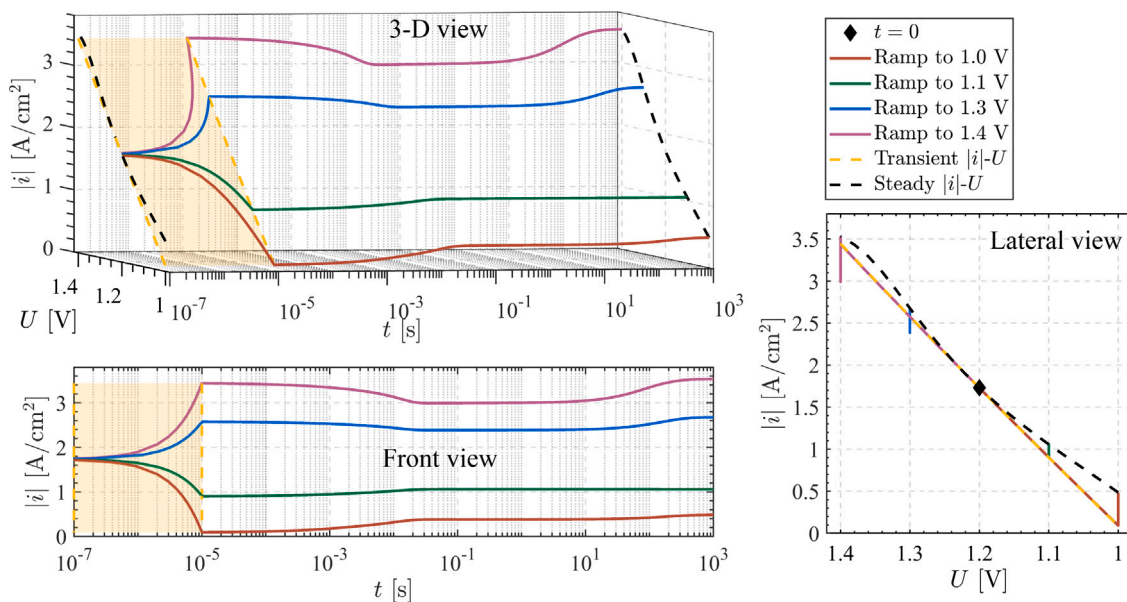


Fig. 6. 3-D demonstration of current density magnitude versus voltage and time. The electrical responses to voltage ramps with different ramp magnitudes (linear ramps from 1.2 V to 1.0 V, 1.1 V, 1.3 V, and 1.4 V, respectively) are presented.

1.1 V, 1.3 V, and 1.4 V, respectively. In addition, the steady-state and transient  $|i| - U$  curves are presented to demonstrate the patterns of current responses. The steady-state  $|i| - U$  curve is obtained from steady simulations by varying the boundary condition of voltage but holding the other boundary conditions unchanged according to Table 2. The transient  $|i| - U$  curve is obtained by varying the voltage but forcing the species concentrations and temperature in FL to be unchanged from their initial values.

As shown in the front view of Fig. 6, after the voltage ramp-down from 1.2 V to 1.1 V or 1.0 V, the current magnitudes monotonically increase to their final steady-state values from 10<sup>-5</sup> s to 10<sup>3</sup> s. By contrast, the trends of current magnitudes decrease first and then increase after the voltage ramp-up from 1.2 V to 1.3 V or 1.4 V. Although having different trends, the responses of current magnitude all undergo a fast relaxation period (10<sup>-5</sup> s to 10<sup>-2</sup> s) and a slow relaxation period (10<sup>1</sup> s to 10<sup>3</sup> s). Such a phenomenon implies that the relaxation time of current responses may be independent of the ramp magnitudes [25].

The lateral view in Fig. 6 displays the similarities of the four current responses in terms of current-voltage characteristic. Specifically, the

four current responses obey the steady-state  $|i| - U$  characteristic at  $t = 0$ , then deviate, and finally recover to the steady-state  $|i| - U$  characteristic at their final steady states. More surprisingly, as highlighted by a yellow panel in Fig. 6, in the first 10<sup>-5</sup> s, the four current responses obey the same transient  $|i| - U$  characteristic although affected by different voltage ramp magnitudes. An explanation to this is that the  $|i| - U$  characteristic of SOEC is heavily depended on the species concentration and temperature in FL as well as the intrinsic ohmic resistance. Since the species concentration and temperature are almost unchanged in the first 10<sup>-5</sup> s due to the heat and mass transfer lags as discussed in Section 3.1, the transient  $|i| - U$  displays ohmic characteristic and a linear slope that is relative to the overall ohmic resistance of SOEC. As the species concentration and temperature develop to a new steady state, the transient  $|i| - U$  characteristic is transformed to the steady-state one. In general, for the SOEC subjected to fast electrical changes, the electrical undershoots or overshoots are the reflection of the discrepancies between the steady-state and transient  $|i| - U$  characteristics.

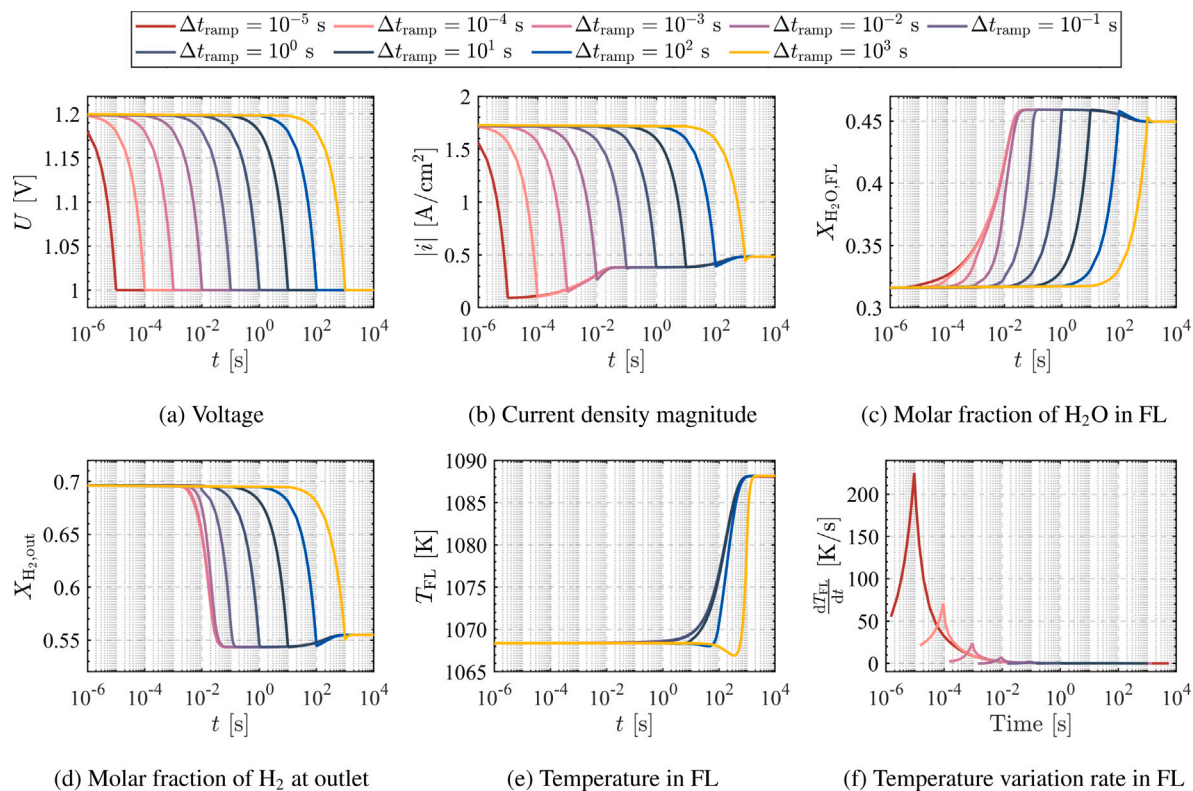


Fig. 7. Illustration of different variables versus time, which show the electrical, molar, and thermal responses to different voltage ramps. Voltage linearly ramps from 1.2 V to 1.0 V in different ramp time  $\Delta t_{\text{ramp}}$ .

### 3.4. Responses to voltage ramps with different ramp rates

To study the influence of ramp rate on dynamic responses of SOEC, simulations with various ramp times ranging from  $10^{-5}$  s to  $10^3$  s are performed. Fig. 7 compares the responses of electrical, molar, and thermal variables to voltage ramps with different ramp time  $\Delta t_{\text{ramp}}$ . Once again, the response of the current density magnitude  $|i|$  confirms that the undershoot of current magnitude is caused by mass-transfer lag and heat-transfer lag. As shown in Fig. 7(b), if the ramp time  $\Delta t_{\text{ramp}}$  is sufficiently short, for example  $\Delta t_{\text{ramp}} \leq 10^{-4}$  s, the curves of molar fraction of  $\text{H}_2\text{O}$  in FL (Fig. 7(c)) and the molar fraction of  $\text{H}_2$  at outlet (Fig. 7(d)) change little when further decreasing  $\Delta t_{\text{ramp}}$ . That implies the mass transfer fails to follow the voltage change. Therefore, slowing down the voltage ramp by increasing the ramp time  $\Delta t_{\text{ramp}}$  from  $10^{-5}$  s to  $10^{-1}$  s can alleviate and even eliminate the undershoot of current density induced by the slow mass transfer (Fig. 7(b)). Similarly, in terms of thermal responses, the temperature of SOEC cannot follow the voltage ramp until  $\Delta t_{\text{ramp}}$  increases to  $10^3$  s (Fig. 7(e)). Thus, it would be highly time-consuming to eliminate the thermal-lag-induced undershoot of current magnitude by merely increasing  $\Delta t_{\text{ramp}}$ . More effective control strategies and structure designs are needed to deal with the severe heat-transfer lag. The accurate time constants of the lags of heat and mass transfer will be determined in Section 3.5.

Besides, slowing down the voltage ramp may benefit the thermal safety of SOEC, as evidenced by the smaller temperature variation rate in FL due to the increase of  $\Delta t_{\text{ramp}}$  in Fig. 7(f). The fast variations of temperature is due to the fact that heat sources of FL are determined by the current (Table 4). And the rapid response of current to voltage variation would certainly lead to the fast variation of heat sources and temperature. Although the temperature variation rate is high, it only lasts for a short time and leads to a limited temperature increase (around 0.05 K in  $10^{-2}$  s) in this case. However, if rapid voltage changes occur to a large-scale SOEC system continuously, potential thermal safety problems such as thermal fatigue should be carefully evaluated.

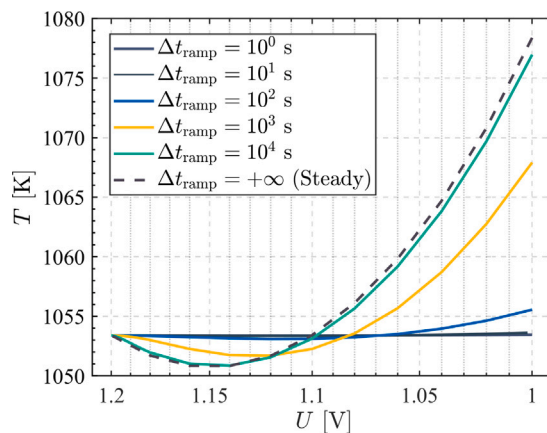


Fig. 8. Temperature of SOEC at different voltages during the voltage ramp..

In the majority of cases in Fig. 7(e), the temperature seems to monotonically increase from the initial state to the final steady state. So, it may be confusing to observe that the temperature decreases first and then increases until the final steady state is reached ( $\Delta t_{\text{ramp}} > 10^2$  s). It should be reminded that the decrease of temperature during the voltage ramp is not an undershoot caused by the mismatch of time constants. Instead, it is due to the non-linearity between the heat sources and the voltage. To prove this viewpoint, the temperature data of SOEC under different voltages are recorded during the voltage ramp. Fig. 8 presents the recorded  $T - U$  curves of the cases with different voltage ramp times. The data of  $\Delta t_{\text{ramp}} = +\infty$  are obtained from steady simulations by varying the boundary condition of voltage and holding the other boundary conditions unchanged according to Table 2. In Fig. 8, the non-linearity between heat source and voltage

is reflected on the  $T - U$  curve when the voltage ramp is sufficiently slow. Physically, the non-linearity is caused by the difference between the entropy change of reaction and the input electrical energy. While for cases with small  $\Delta t_{\text{ramp}}$ , voltage ramps rapidly and the non-linearity of heat sources during the voltage ramp is negligible. Consequently, during fast voltage ramps, the  $T - U$  curve is almost flat in Fig. 8 and the  $T_{\text{FL}} - t$  curves are monotonic between the initial state and final state in Fig. 7(e).

### 3.5. Quantification of time constants for heat and mass transfer

As discussed in Section 3.1, the species concentrations and temperature in FL directly affect the current of SOEC. Therefore, the molar and thermal responses in FL are of interest when quantifying the transient electrical behaviors of SOEC. This section determines the time constants of heat and mass transfer in FL.

As shown in Fig. 7, when the voltage ramp time  $\Delta t_{\text{ramp}}$  decreases to  $10^{-5}$  s, a further decrease of  $\Delta t_{\text{ramp}}$  will have little effects on the shapes of  $X_{\text{H}_2\text{O,FL}} - t$  curve and  $T_{\text{FL}} - t$  curve since the mass transfer rate and heat transfer rate have reached their maximums. More precisely, when the voltage ramps from 1.2 V to 1.0 V in  $10^{-5}$  s, the response of molar concentration of species from  $10^{-5}$  s to  $10^{-1}$  s (from  $t_{\text{ramp}}$  to  $t_{\text{quasi}}$ ) and the response of temperature from  $10^{-5}$  s to  $10^3$  s (from  $t_{\text{ramp}}$  to  $t_{\text{steady}}$ ) in FL can be considered as step responses. The responses of mole fraction and temperature can be normalized according to Eq. (20) and (21), respectively.

$$\Delta X_i^* = \frac{X_i - X_i|_{t=t_{\text{quasi}}}}{X_i|_{t=0} - X_i|_{t=t_{\text{quasi}}}} \quad (20)$$

$$\Delta T^* = \frac{T - T|_{t=t_{\text{steady}}}}{T|_{t=0} - T|_{t=t_{\text{steady}}}} \quad (21)$$

The normalized variables are plotted against time in Fig. 9. Interestingly, the responses of the normalized terms  $\Delta X_i^*$  and  $\Delta T^*$  approximate to the unit-step response of linear time-invariant systems [45]. Hence, the responses of  $\Delta X_i^*$  and  $\Delta T^*$  can be fitted according to Eq. (22) and (23) [45] to obtain the time constants of molar and thermal responses in FL.

$$\Delta X_i^* \approx e^{-\frac{t}{\tau_{m,i}}} \quad (22)$$

$$\Delta T^* \approx e^{-\frac{t}{\tau_t}} \quad (23)$$

where,  $\tau_{m,i}$  is the time constant of the molar response of species  $i$  and the  $\tau_t$  is the time constant of thermal response. The fitted time constants are  $\tau_{m,\text{H}_2\text{O,FL}} = \tau_{m,\text{H}_2,\text{FL}} = 0.00723$  s,  $\tau_{m,\text{O}_2,\text{FL}} = 0.00133$  s, and  $\tau_{t,\text{FL}} = 180$  s. Considering Eqs. (20)~(23) and the fact that  $\exp(-3) \approx 0.05$ , the molar and temperature fields requires  $3\tau$  to finish 95% transition from initial state to steady state. And a more thorough transition of 99.3% will require  $5\tau$ , given that  $\exp(-5) \approx 0.007$ . So, it can be estimated that the time required for the fast relaxation (governed by mass transfer) approximates  $5\tau_{m,\text{H}_2\text{O,FL}} = 0.036$  s, and the time required for the slow relaxation (governed by heat transfer) approximates  $5\tau_{t,\text{FL}} = 900$  s. These estimations are consistent with the simulation results presented in Fig. 3.

When comparing the fitted time constants, it is apparent that the time constant of heat transfer is around  $10^5$  times larger than that of mass transfer. Referring to the estimated time constants in each component of SOEC (Table 5), the large thermal time constant may be attributed to the slow heat conduction within the interconnect in the length direction ( $\tau_{t,\text{diff},L} = 830$  s). On one hand, unlike the porous components and fluid channels where both heat conduction and convective heat transfer are effective, the interconnect is a solid part within which conduction is the only way for heat transfer. On the other hand, the interconnect occupies about 75% of the total volume of the investigated SOEC. So, the time constant of heat conduction in the interconnect may play a decisive role in the thermal response of the

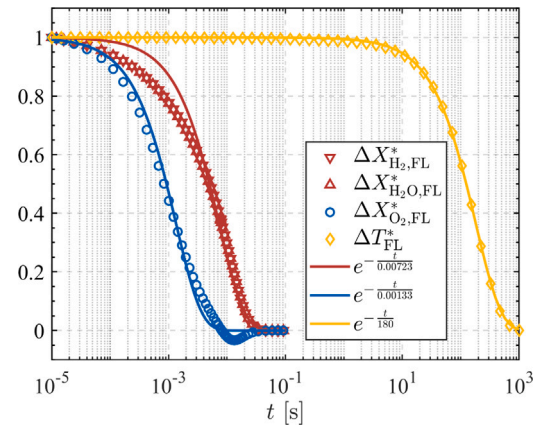


Fig. 9. Fittings between the molar and thermal responses (under a voltage ramp from 1.2 V to 1.0 V in  $10^{-5}$  s in the FL) and the unit-step response of linear time-invariant system.

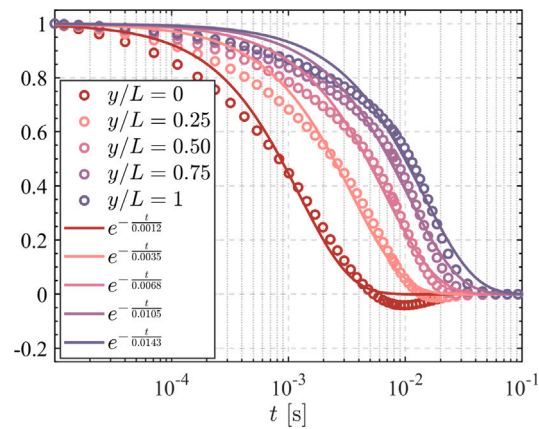


Fig. 10. Fittings between responses of  $\text{H}_2\text{O}$  molar fraction at different stream-wise positions in the FL of SOEC with the unit-step response of linear time-invariant system.

SOEC. To reduce the heat-transfer lag, it is of importance to optimize the design of interconnect for faster heat conduction.

As for the larger time constant of  $\text{H}_2$  and  $\text{H}_2\text{O}$  compared to that of  $\text{O}_2$ , it may be due to the much larger thickness and time constant of fuel DL ( $\tau_{m,\text{diff},\text{FuelDL},\delta} = 2.1 \times 10^{-2}$  s) that hinder the diffusion of  $\text{H}_2$  and  $\text{H}_2\text{O}$  from channel to FL. Besides, in Fig. 9, the data points of  $\text{H}_2$  and  $\text{H}_2\text{O}$  overlap because the diffusivity of  $\text{H}_2$  and  $\text{H}_2\text{O}$  are almost the same in a binary diffusion. In addition, the curve of  $\Delta X_{\text{O}_2,\text{FL}}^*$  undergoes an undershoot and then reaches zero together with  $\Delta X_{\text{H}_2,\text{FL}}^*$  and  $\Delta X_{\text{H}_2\text{O,FL}}^*$ . The undershoot of  $\Delta X_{\text{O}_2,\text{FL}}^*$  may be caused by the difference between  $\tau_{m,\text{O}_2,\text{FL}}$  and  $\tau_{m,\text{H}_2\text{O,FL}}$ .

Only relying on the limited data in this study, it is difficult to propose a general formula to estimate the time constants of heat and mass transfer in FL based on the time constants listed in Table 5. While some interesting facts about mass transfer time constants can be observed from the comparison of the fitted  $\tau_{m,\text{H}_2\text{O}}$  at different  $y$  coordinates along the channel in the FL, as shown in Fig. 10. Firstly, by looking at the legend, the fitted  $\tau_{m,\text{H}_2\text{O}}$  increases with the  $y$  coordinate almost linearly. Secondly, when comparing the fitted  $\tau_{m,\text{H}_2\text{O}}$  at the inlet ( $y/L = 0$ , no advection lag) and that at the outlet ( $y/L = 1$ , the highest advection lag), it is clear that the difference between them, which is 0.0131 s, approximates the advection time constant ( $\tau_{\text{advec},L} = 0.012$  s) listed in Table 5. Considering that the advection lag is linear with  $y$  coordinate, the average advection lag imposed on the whole FL should be half of the advection time constant ( $\tau_{\text{advec},L}/2 = 0.006$  s), which is just slightly smaller than the fitted time constant of  $\text{H}_2\text{O}$  variation in

**Table 5**Estimated time constants for heat and mass transfer in different components of SOEC under  $T = 1123\text{ K}$  and  $p = 1\text{ atm}$ .

	Fuel			Electrolyte	Air			Interconnect
	Channel	DL	FL		Channel	DL	FL	
$\tau_{m,diff,\delta}$ [s] <sup>a</sup>	$1.4 \times 10^{-3}$	$2.1 \times 10^{-2}$	$1.0 \times 10^{-6}$	N.A.N.	$6.1 \times 10^{-3}$	$2.0 \times 10^{-4}$	$4.9 \times 10^{-6}$	N.A.N.
$\tau_{t,diff,\delta}$ [s] <sup>b</sup>	$1.6 \times 10^{-3}$	$2.5 \times 10^{-1}$	$1.2 \times 10^{-5}$	$1.2 \times 10^{-4}$	$5.0 \times 10^{-3}$	$1.3 \times 10^{-3}$	$3.2 \times 10^{-5}$	$8.3 \times 10^{-2}$
$\tau_{m,diff,L}$ [s] <sup>c</sup>	$1.4 \times 10^1$	$2.1 \times 10^2$	$2.1 \times 10^2$	N.A.N.	$6.1 \times 10^1$	$1.0 \times 10^3$	$1.0 \times 10^3$	N.A.N.
$\tau_{t,diff,L}$ [s] <sup>d</sup>	$1.6 \times 10^1$	$2.5 \times 10^3$	$2.5 \times 10^3$	$1.2 \times 10^4$	$5.0 \times 10^1$	$6.5 \times 10^3$	$6.5 \times 10^3$	$8.3 \times 10^2$
$\tau_{advec,L}$ [s] <sup>e</sup>	$1.2 \times 10^{-2}$	N.E.	N.E.	N.A.N.	$1.2 \times 10^{-2}$	N.E.	N.E.	N.A.N.

N.E. means not evaluated.

N.A.N. means not a number.

<sup>a</sup>Time constant of mass diffusion in thickness direction is estimated by  $\tau_{m,diff,\delta} = \delta^2/D$ .<sup>b</sup>Time constant of thermal diffusion in thickness direction is estimated by  $\tau_{t,diff,\delta} = \delta^2 \rho c_p / k$ .<sup>c</sup>Time constant of mass diffusion in length direction is estimated by  $\tau_{m,diff,L} = L^2/D$ .<sup>d</sup>Time constant of thermal diffusion in length direction is estimated by  $\tau_{t,diff,L} = L^2 \rho c_p / k$ .<sup>e</sup>Time constant of advection is estimated by  $\tau_{advec,L} = L/v$ .**Table A.1**

Material parameters used in the governing equations.

Parameters	Value	Unit	Ref.
Ionic conductivity	$\bar{\sigma}_{CFL}$	2.8	S/m [34]
	$\bar{\sigma}_{AFL}$	5.0	S/m [34]
	$\bar{\sigma}_E$	$\bar{\sigma}_E \cdot \frac{4.19 \times 10^{12}}{T} e^{-\frac{E}{9010}}$	S/m [35]
Electronic conductivity	$\sigma_{Int}$	870000	S/m [34]
	$\sigma_{CDL}$	1773200	S/m [34]
	$\sigma_{CFL}$	2288000	S/m [34]
	$\sigma_{ADL}$	7300	S/m [34]
	$\sigma_{AFL}$	3650	S/m [34]
Thermal conductivity	$k_{Int}$	20	W/m K [34]
	$k_{CDL}$	6	W/m K [34]
	$k_{CFL}$	6	W/m K [34]
	$k_{ADL}$	2	W/m K [34]
	$k_{AFL}$	2	W/m K [34]
	$k_E$	2	W/m K [34]
Porosity	$\epsilon_{CDL}$	0.38	- [34]
	$\epsilon_{CFL}$	0.2	- [34]
	$\epsilon_{ADL}$	0.27	- [34]
	$\epsilon_{AFL}$	0.27	- [34]
Density	$\rho_{CDL}$	3310	kg/m <sup>3</sup> [16]
	$\rho_{CFL}$	3310	kg/m <sup>3</sup> [16]
	$\rho_{ADL}$	3030	kg/m <sup>3</sup> [16]
	$\rho_{AFL}$	3030	kg/m <sup>3</sup> [16]
	$\rho_E$	5160	kg/m <sup>3</sup> [16]
	$\rho_{Int}$	3030	kg/m <sup>3</sup> [16]
Thermal capacity	$c_{p,CDL}$	450	J/kg K [16]
	$c_{p,CFL}$	450	J/kg K [16]
	$c_{p,ADL}$	430	J/kg K [16]
	$c_{p,AFL}$	430	J/kg K [16]
	$c_{p,E}$	470	J/kg K [16]
	$c_{p,Int}$	550	J/kg K [16]

<sup>a</sup>The ionic conductivity of electrolyte is calculated based on the overall ohmic resistance measured by Njodzefon et al. [35].**Table A.2**

Parameters for electrochemical model.

Parameters	Value	Unit	Acquisition
$\zeta_{cat}$	$5.7 \times 10^5$	1/m	Fitted
$\zeta_{an}$	$5.7 \times 10^5$	1/m	Fitted
$a$	-0.10	-	[43]
$b$	0.33	-	[43]
$m$	0.22	-	[43]
$\gamma_{cat}$	$1.82527 \times 10^6 \times T$	A/m <sup>2</sup>	[43]
$\gamma_{an}$	$1.51556 \times 10^8 \times T$	A/m <sup>2</sup>	[43]
$E_{act,cat}$	105.04	kJ/mol	[43]
$E_{act,an}$	139.86	kJ/mol	[43]
$\alpha_{cat}$	0.59	-	[43]
$\alpha_{an}$	0.65	-	[43]

FL ( $\tau_{m,H_2O,FL} = 0.00723\text{ s}$ ). Hence, we may infer that the advection lag plays a dominant role in the variation of H<sub>2</sub>O molar concentration in

FL. To reduce the advection lag, efforts should be put into the design of channel and the control strategy with regards to flow velocity.

Overall, in this section, the time constants of heat and mass transfer in FL are quantified, which are found to be highly correlated with the electrical responses of SOEC. The quantitative and physical understanding of the dynamic characteristics of SOEC provides a solid foundation to further improve the response speed of SOEC via optimizations of structure design and dynamic control.

#### 4. Conclusions

To provide a theoretical basis for the dynamic coupling between SOEC with intermittent renewable power sources, simulations that resolve time scales from  $10^{-6}\text{ s}$  to  $10^4\text{ s}$  are conducted to investigate the electrical, molar, and thermal responses of SOEC to different voltage ramps. Simulation results demonstrate that the current overshoots or undershoots after rapid voltage changes are caused by the mismatch of transfer rates in SOEC, i.e., electronic and ionic charge transfer rates  $>$  mass transfer rate  $>$  heat transfer rate. The electrical overshoots or undershoots are the reflection of the discrepancies between the steady-state and transient current-voltage characteristics and may result in unsteady hydrogen production rate in practice. By merely increasing the voltage ramp time, it is effective to alleviate and even eliminate the electrical overshoots or undershoots induced by mass-transfer lag but it is time-consuming to alleviate those induced by heat-transfer lag. Furthermore, the time constants of heat and mass transfer in the SOEC are quantified in a new way — by fitting the responses of temperature and species in the functional layer with the unit-step responses of linear time-invariant systems. Fitted mass-transfer and heat-transfer time constants in functional layers are  $\tau_{m,H_2O,FL} = \tau_{m,H_2,FL} = 0.00723\text{ s}$ ,  $\tau_{m,O_2,FL} = 0.00133\text{ s}$ , and  $\tau_{t,FL} = 180\text{ s}$ . The advection lag may dominate the mass-transfer time constants. And the slow conduction within the interconnect may be the reason for the large heat-transfer time constant. Besides, the relaxation time of heat and mass transfer can be estimated from the corresponding time constants. The methodology and conclusions presented in this study are applicable for SOEC with similar structures. The improved understanding of the transient characteristics is believed to be beneficial for control systems, structure design, and operation safety of SOEC.

#### CRedit authorship contribution statement

**Zhaojian Liang:** Conceptualization, Methodology, Software, Formal analysis, Writing – original draft. **Jingyi Wang:** Writing – review & editing, Funding acquisition, Investigation. **Yang Wang:** Methodology, Software. **Meng Ni:** Writing – review & editing, Methodology. **Mengying Li:** Formal analysis, Writing – review & editing, Supervision, Funding acquisition.

## Declaration of competing interest

The authors declare that they have no known competing financial interests or personal relationships that could have appeared to influence the work reported in this paper.

## Data availability

Data will be made available on request.

## Acknowledgments

The authors gratefully acknowledge the partial support from the Hong Kong Polytechnic University, Hong Kong (P0035016), the partial support from Shenzhen Finance Bureau (HA11409053), and the partial support from Department of Education of Guangdong Province, China (2021KQNCX271).

## Appendix A. Supplementary materials

See Tables A.1 and A.2.

## Appendix B. Supplementary data

Supplementary material related to this article can be found online at <https://doi.org/10.1016/j.enconman.2023.116759>.

## References

- [1] BP plc. BP statistical review of world energy 2021. 2021, URL <https://www.bp.com/en/global/corporate/energy-economics/statistical-review-of-world-energy.html>.
- [2] Xu Q, Guo Z, Xia L, He Q, Li Z, Temitope Bello I, Zheng K, Ni M. A comprehensive review of solid oxide fuel cells operating on various promising alternative fuels. *Energy Convers Manage* 2022;253:115175. <http://dx.doi.org/10.1016/j.enconman.2021.115175>, URL <https://www.sciencedirect.com/science/article/pii/S0196890421013510>.
- [3] Wang H, Kong H, Pu Z, Li Y, Hu X. Feasibility of high efficient solar hydrogen generation system integrating photovoltaic cell/photon-enhanced thermionic emission and high-temperature electrolysis cell. *Energy Convers Manage* 2020;210:112699. <http://dx.doi.org/10.1016/j.enconman.2020.112699>, URL <https://www.sciencedirect.com/science/article/pii/S0196890420302375>.
- [4] Schiller G, Lang M, Szabo P, Monnerie N, von Storch H, Reinhold J, Sundarraj P. Solar heat integrated solid oxide steam electrolysis for highly efficient hydrogen production. *J Power Sources* 2019;416:72–8. <http://dx.doi.org/10.1016/j.jpowsour.2019.01.059>, URL <https://www.sciencedirect.com/science/article/pii/S0378775319300710>.
- [5] Sanz-Bermejo J, Muñoz-Antón J, Gonzalez-Aguilar J, Romero M. Optimal integration of a solid-oxide electrolyser cell into a direct steam generation solar tower plant for zero-emission hydrogen production. *Appl Energy* 2014;131:238–47. <http://dx.doi.org/10.1016/j.apenergy.2014.06.028>, URL <https://www.sciencedirect.com/science/article/pii/S0360261914006102>.
- [6] IEA. IEA hydrogen projects database 2021. 2021, URL <https://www.iea.org/data-and-statistics/data-product/hydrogen-projects-database>.
- [7] Cai Q, Adjiman CS, Brandon NP. Optimal control strategies for hydrogen production when coupling solid oxide electrolyzers with intermittent renewable energies. *J Power Sources* 2014;268:212–24. <http://dx.doi.org/10.1016/j.jpowsour.2014.06.028>, URL <https://www.sciencedirect.com/science/article/pii/S0378775314008817>.
- [8] Restrepo JC, Luis Izidoro D, Milena Lozano Násner A, José Venturini O, Eduardo Silva Lora E. Techno-economical evaluation of renewable hydrogen production through concentrated solar energy. *Energy Convers Manage* 2022;258:115372. <http://dx.doi.org/10.1016/j.enconman.2022.115372>, URL <https://www.sciencedirect.com/science/article/pii/S0196890422001686>.
- [9] Liu G, Zhao W, Li Z, Xia Z, Jiang C, Kupecki J, Pang S, Deng Z, Li X. Modeling and control-oriented thermal safety analysis for mode switching process of reversible solid oxide cell system. *Energy Convers Manage* 2022;255:115318. <http://dx.doi.org/10.1016/j.enconman.2022.115318>, URL <https://www.sciencedirect.com/science/article/pii/S0196890422001145>.
- [10] Wang Y, Wu C, Zhao S, Guo Z, Zu B, Han M, Du Q, Ni M, Jiao K. Assessing performance degradation induced by thermal cycling in solid oxide cells. *Energy Convers Manage* 2022;270:116239. <http://dx.doi.org/10.1016/j.enconman.2022.116239>, URL <https://www.sciencedirect.com/science/article/pii/S0196890422010160>.
- [11] Eichhorn Colombo KW, Kharton VV, Berto F, Paltrinieri N. Mathematical modeling and simulation of hydrogen-fueled solid oxide fuel cell system for micro-grid applications - Effect of failure and degradation on transient performance. *Energy* 2020;202:117752. <http://dx.doi.org/10.1016/j.energy.2020.117752>, URL <https://www.sciencedirect.com/science/article/pii/S0360544220308598>.
- [12] Xia Z, Deng Z, Jiang C, qi Zhao D, Kupecki J, long Wu X, wu Xu Y, qiang Liu G, Fu X, Li X. Modeling and analysis of cross-flow solid oxide electrolysis cell with oxygen electrode/electrolyte interface oxygen pressure characteristics for hydrogen production. *J Power Sources* 2022;529:231248. <http://dx.doi.org/10.1016/j.jpowsour.2022.231248>.
- [13] Bae Y, Lee S, Hong J. The effect of anode microstructure and fuel utilization on current relaxation and concentration polarization of solid oxide fuel cell under electrical load change. *Energy Convers Manage* 2019;201:112152. <http://dx.doi.org/10.1016/j.enconman.2019.112152>, URL <https://www.sciencedirect.com/science/article/pii/S0196890419311586>.
- [14] Jia J, Seitz LC, Benck JD, Huo Y, Chen Y, Ng JWD, Bilir T, Harris JS, Jaramillo TF. Solar water splitting by photovoltaic-electrolysis with a solar-to-hydrogen efficiency over 30%. *Nature Commun* 2016;7(1):13237. <http://dx.doi.org/10.1038/ncomms13237>, URL <http://www.nature.com/articles/ncomms13237>.
- [15] Wang Y, Du Y, Ni M, Zhan R, Du Q, Jiao K. Three-dimensional modeling of flow field optimization for co-electrolysis solid oxide electrolysis cell. *Appl Therm Eng* 2020;172:114959. <http://dx.doi.org/10.1016/j.applthermaleng.2020.114959>, URL <https://www.sciencedirect.com/science/article/pii/S1359431119362192>.
- [16] Wang Y, Zhan R, Qin Y, Zhang G, Du Q, Jiao K. Three-dimensional modeling of pressure effect on operating characteristics and performance of solid oxide fuel cell. *Int J Hydrog Energy* 2018;43(43):20059–76. <http://dx.doi.org/10.1016/j.ijhydene.2018.09.025>.
- [17] Ni M. Modeling of a solid oxide electrolysis cell for carbon dioxide electrolysis. *Chem Eng J* 2010;164(1):246–54. <http://dx.doi.org/10.1016/j.cej.2010.08.032>, URL <https://www.sciencedirect.com/science/article/pii/S1385894710007370>.
- [18] Bhattacharyya D, Rengaswamy R, Finnerty C. Dynamic modeling and validation studies of a tubular solid oxide fuel cell. *Chem Eng Sci* 2009;64(9):2158–72. <http://dx.doi.org/10.1016/j.ces.2008.12.040>, URL <https://www.sciencedirect.com/science/article/pii/S0009250908007008>.
- [19] Komatsu Y, Brus G, Kimijima S, Szym J. The effect of overpotentials on the transient response of the 300W SOFC cell stack voltage. *Appl Energy* 2014;115:352–9. <http://dx.doi.org/10.1016/j.apenergy.2013.11.017>, URL <https://www.sciencedirect.com/science/article/pii/S0360261913009100>.
- [20] Petipas F, Fu Q, Brisse A, Bouallou C. Transient operation of a solid oxide electrolysis cell. *Int J Hydrogen Energy* 2013;38(7):2957–64. <http://dx.doi.org/10.1016/j.ijhydene.2012.12.086>, URL <https://www.sciencedirect.com/science/article/pii/S0360319912027899>.
- [21] Preiner M, Stoeckl B, Subotić V, Mittmann F, Hochenauer C. Performance of a ten-layer reversible Solid Oxide Cell stack (rSOC) under transient operation for autonomous application. *Appl Energy* 2019;254:113695. <http://dx.doi.org/10.1016/j.apenergy.2019.113695>, URL <https://www.sciencedirect.com/science/article/pii/S0360261919313820>.
- [22] Fogel S, Kryk H, Hampel U. Simulation of the transient behavior of tubular solid oxide electrolyzer cells under fast load variations. *Int J Hydrogen Energy* 2019;44(18):9188–202. <http://dx.doi.org/10.1016/j.ijhydene.2019.02.063>, URL <https://www.sciencedirect.com/science/article/pii/S0360319919306470>.
- [23] Gemmen RS, Johnson CD. Effect of load transients on SOFC operation—current reversal on loss of load. *J Power Sources* 2005;144(1):152–64. <http://dx.doi.org/10.1016/j.jpowsour.2004.12.027>, URL <https://www.sciencedirect.com/science/article/pii/S0378775305000157>.
- [24] Qi Y, Huang B, Chuang KT. Dynamic modeling of solid oxide fuel cell: The effect of diffusion and inherent impedance. *J Power Sources* 2005;150:32–47. <http://dx.doi.org/10.1016/j.jpowsour.2005.02.080>, URL <https://www.sciencedirect.com/science/article/pii/S0378775305002363>.
- [25] Serincan MF, Pasaogullari U, Sannes NM. A transient analysis of a micro-tubular solid oxide fuel cell (SOFC). *J Power Sources* 2009;194(2):864–72. <http://dx.doi.org/10.1016/j.jpowsour.2009.06.036>, URL <https://www.sciencedirect.com/science/article/pii/S0378775309010519>.
- [26] Jin X, Xue X. Mathematical modeling analysis of regenerative solid oxide fuel cells in switching mode conditions. *J Power Sources* 2010;195(19):6652–8. <http://dx.doi.org/10.1016/j.jpowsour.2010.04.018>, URL <https://www.sciencedirect.com/science/article/pii/S0378775310006440>.
- [27] Nerat M. Modeling and analysis of short-period transient response of a single, planar, anode supported, solid oxide fuel cell during load variations. *Energy* 2017;138:728–38. <http://dx.doi.org/10.1016/j.energy.2017.07.133>, URL <https://www.sciencedirect.com/science/article/pii/S0360544217313166>.
- [28] Bae Y, Lee S, Yoon KJ, Lee J-H, Hong J. Three-dimensional dynamic modeling and transport analysis of solid oxide fuel cells under electrical load change. *Energy Convers Manage* 2018;165:405–18. <http://dx.doi.org/10.1016/j.enconman.2018.03.064>, URL <https://www.sciencedirect.com/science/article/pii/S0196890418302930>.
- [29] Aguiar P, Adjiman C, Brandon N. Anode-supported intermediate-temperature direct internal reforming solid oxide fuel cell: II. Model-based dynamic performance and control. *J Power Sources* 2005;147(1):136–47. <http://dx.doi.org/10.1016/>

- j.jpowsour.2005.01.017, URL <https://www.sciencedirect.com/science/article/pii/S0378775305001473>.
- [30] Udagawa J, Aguiar P, Brandon N. Hydrogen production through steam electrolysis: Model-based dynamic behaviour of a cathode-supported intermediate temperature solid oxide electrolysis cell. *J Power Sources* 2008;180(1):46–55. <http://dx.doi.org/10.1016/j.jpowsour.2008.02.026>, URL <https://www.sciencedirect.com/science/article/pii/S0378775308003716>.
- [31] Luo Y, Shi Y, Li W, Cai N. Dynamic electro-thermal modeling of co-electrolysis of steam and carbon dioxide in a tubular solid oxide electrolysis cell. *Energy* 2015;89:637–47. <http://dx.doi.org/10.1016/j.energy.2015.05.150>, URL <https://www.sciencedirect.com/science/article/pii/S0360544215007793>.
- [32] Banerjee A, Wang Y, Diercks J, Deutschmann O. Hierarchical modeling of solid oxide cells and stacks producing syngas via H<sub>2</sub>O/CO<sub>2</sub> Co-electrolysis for industrial applications. *Appl Energy* 2018;230:996–1013. <http://dx.doi.org/10.1016/j.apenergy.2018.08.122>, URL <https://www.sciencedirect.com/science/article/pii/S0360261918312960>.
- [33] Albrecht KJ, Braun RJ. The effect of coupled mass transport and internal reforming on modeling of solid oxide fuel cells part II: Benchmarking transient response and dynamic model fidelity assessment. *J Power Sources* 2016;304:402–8. <http://dx.doi.org/10.1016/j.jpowsour.2015.07.087>, URL <https://www.sciencedirect.com/science/article/pii/S0378775315301373>.
- [34] Lee S, Kim H, Yoon KJ, Son J-W, Lee J-H, Kim B-K, Choi W, Hong J. The effect of fuel utilization on heat and mass transfer within solid oxide fuel cells examined by three-dimensional numerical simulations. *Int J Heat Mass Transfer* 2016;97:77–93. <http://dx.doi.org/10.1016/j.ijheatmasstransfer.2016.02.001>.
- [35] Njodzefon J-C, Klotz D, Kromp A, Weber A, Ivers-Tiffée E. Electrochemical modeling of the current-voltage characteristics of an SOFC in fuel cell and electrolyzer operation modes. *J Electrochem Soc* 2013;160(4):F313. <http://dx.doi.org/10.1149/2.018304jes>.
- [36] Beale SB, Andersson M, Boigues-Muñoz C, Frandsen HL, Lin Z, McPhail SJ, Ni M, Sundén B, Weber A, Weber AZ. Continuum scale modelling and complementary experimentation of solid oxide cells. *Prog Energy Combust Sci* 2021;85:100902. <http://dx.doi.org/10.1016/j.pecs.2020.100902>, URL <https://www.sciencedirect.com/science/article/pii/S036012852030112X>.
- [37] García-Camprubí M, Izquierdo S, Fueyo N. Challenges in the electrochemical modelling of solid oxide fuel and electrolyser cells. *Renew Sustain Energy Rev* 2014;33:701–18. <http://dx.doi.org/10.1016/j.rser.2014.02.034>.
- [38] Manual AF. ANSYS FLUENT advanced add-on modules. ANSYS. 2015.
- [39] Resch E, Pharoah J. Numerical and experimental characterisation of convective transport in solid oxide fuel cells [Master's thesis], Kingston, Ontario, Canada: Queen's University; 2008, URL <https://qspace.library.queensu.ca/handle/1974/1576>.
- [40] NIST. Thermophysical properties of fluid systems. 2021, URL <https://webbook.nist.gov/chemistry/fluid/>.
- [41] Cussler EL, Cussler EL. Diffusion: mass transfer in fluid systems. Cambridge University Press; 2009.
- [42] Leonide A, Sonn V, Weber A, Ivers-Tiffée E. Evaluation and modeling of the cell resistance in anode-supported solid oxide fuel cells. *J Electrochem Soc* 2007;155(1):B36. <http://dx.doi.org/10.1149/1.2801372>.
- [43] Leonide A, Apel Y, Ivers-Tiffée E. SOFC modeling and parameter identification by means of impedance spectroscopy. *ECS Trans* 2009;19(20):81. <http://dx.doi.org/10.1149/1.3247567>.
- [44] Jiao K, Li X. Water transport in polymer electrolyte membrane fuel cells. *Prog Energy Combust Sci* 2011;37(3):221–91. <http://dx.doi.org/10.1016/j.pecs.2010.06.002>, URL <https://www.sciencedirect.com/science/article/pii/S0360128510000511>.
- [45] Ogata K, et al. Modern control engineering. vol. 5, NJ: Prentice hall Upper Saddle River; 2010.